Journal of Power Electronics (2021) 21:1633–1645
https://doi.org/10.1007/s43236-021-00308-7

ORIGINAL ARTICLE

Integrated multifunctional power converter for small electric vehicles

He Cheng[1] · Wuhui Wang[1] · Hailong Liu[1] · Shiyang Yang[1]

Received: 27 March 2021 / Revised: 30 August 2021 / Accepted: 1 September 2021 / Published online: 14 September 2021

Abstract
This paper proposes an integrated multifunctional power converter topology, where a traction battery charger (TBC), an auxiliary battery charger (ABC), and a motor drive converter (MDC) merge into an effective system. Traction battery charging, auxiliary battery charging, and motor driving operation modes can be realized by sharing power components. For the battery charging mode, a single-phase power supply charges the traction battery, and the circuit is capable of power factor correction (PFC) and active power decoupling (APD) (G2V mode). For the purpose of enhancing its charging power, the traction battery can also be connected to a three-phase power supply. For the battery discharging mode, the traction battery can feed energy back to a single-phase grid or a three-phase grid (V2G mode). When necessary, the traction battery can charge an auxiliary battery through a DC–DC converter (T2A mode). In the motor driving mode, the energy of the traction battery is used to drive a motor (T2M mode). Each of the charging modes can be implemented under the galvanic isolated condition. Power relays are used to switch the operating modes of the proposed topology.

Keywords Traction battery charger · Auxiliary battery charger · Motor drive converter · Integrated · Multifunctional

1 Introduction

Electric vehicles (EVs) have many advantages over conventional internal combustion engine vehicles, such as low carbon emissions, environmental protection, low maintenance and reduced use cost. As a result, they have attracted a great deal of attention all over the world [1, 2]. At the same time, small electric vehicles have received special attention due to their simple operation, low operation voltage, low price, and small size, which can relieve the pressures of traffic and parking in urban areas [3, 4]. Battery chargers are indispensable for EVs. Based on their installation methods, battery chargers are mainly divided into two categories. The first category includes off-board chargers installed at dedicated charging stations. A large number of off-board charger topologies have been introduced in [5]. The other category includes on-board chargers that can be directly connected to power outlets, which are more convenient for users. Therefore, on-board chargers have been become a major research focus [6].

On-board chargers usually adopt a two-stage structure. The front stage is an AC–DC converter that is used to provide stable DC power to the battery and has power factor correction capabilities. The rear stage is a DC–DC converter, which is used to ensure galvanic isolation [7]. In addition, an auxiliary battery charger (ABC) is required to charge the auxiliary batteries that are used to supply power to headlights, music players, and other electronic devices [8]. For the purpose of safety, galvanic isolation should be ensured among the power grid, traction battery, and auxiliary battery. Some common AC–DC and DC–DC converter topologies were introduced in [9]. For EVs, the internal space is very limited. Therefore, multiple functions integrated into one system with a small size and high reliability are favored. To this end, many papers have proposed integrated multifunctional on-board charger topologies [8–12]. A single-phase reconfigurable on-board charger was presented in [8]. Both a traction battery charger and an auxiliary battery charger are integrated into this charger, and its structure is relatively simple. A transformer is used to isolate the auxiliary battery from the traction battery. However, there is no galvanic isolation between the grid and the traction battery, which reduces the safety of the system. In [10], a multifunctional on-board charger was proposed that can realize a bidirectional energy flow. An LLC resonant converter was adopted to ensure

✉ He Cheng
chenghecumt@163.com

[1] School of Electrical and Power Engineering, China University of Mining and Technology, Jiangsu, China

galvanic isolation. However, a bulky capacitor was used to eliminate the second-order ripple power, which increased the volume of the device. An integrated three-phase on-board charger was proposed in [12]. Motor windings were used as inductors for charging. However, additional contactors were required to switch the operation modes, and galvanic isolation between the battery and the grid is not achievable. Different on-board charger topologies and their corresponding control schemes were presented in [13, 14]. These chargers either lack galvanic isolation capability or a low integration level, which leads to insecurity, large device size, and increased cost.

It is hoped that both the single-phase and three-phase charging modes can be implemented by an on-board charger. Previous studies tend to focus on one of them. When compared with a three-phase charger, a single-phase charger has fewer components, a smaller volume, and a lower cost. However, for single-phase systems, the inherent second-order ripple power is a serious problem. To eliminate ripple power, a method of connecting a bulk electrolytic capacitor to a DC-link is usually adopted. However, this simultaneously increases the volume of the device. For this reason, some active power decoupling (APD) methods have been suggested in [15–18]. However, additional switches are used in these methods.

In this paper, a power converter topology with high integration and multiple operation modes is proposed. The proposed topology is suitable for small electric vehicles that integrate a traction battery charger (TBC), an auxiliary battery charger (ABC), and a motor driving converter (MDC). The proposed topology can be configured to single-phase or three-phase modes. The traction battery can be charged by linking it to a single-phase power supply [G2V(1P)], with active power decoupling (APD) and power factor correction capability (PFC). The traction battery can also be connected to a three-phase power supply to enhance the charging power [G2V(3P)]. In addition, the energy stored in the traction battery can be fed back to a single-phase grid [V2G(1P)] or a three-phase grid [V2G(3P)]. The traction battery can supply power to the auxiliary battery (T2A). When an electric vehicle is running, the traction battery is discharged to drive the motor (T2M). The proposed topology can be configured in four modes (G2V, V2G, T2A, and T2M) and has good galvanic isolation capability.

This paper mainly consists of six parts. Section 2 introduces the overall structure of the proposed topology, followed by a detailed analysis of the operation modes. The control strategies and design parameters are discussed in Sect. 3. Section 4 introduces experimental results obtained under four modes, and verifies the effectiveness of the proposed topology. In Sect. 5, the proposed topology is compared with some common topologies. Finally, Sect. 6 summarizes the work of this paper and draws some conclusions.

2 Proposed powertrain topology

2.1 Structure of the proposed topology

A schematic diagram of an electrical powertrain and an on-board charger is illustrated in Fig. 1. Obviously, the traction battery charger (TBC) consists of an isolated DC–DC converter and an AC–DC converter. The auxiliary battery charger (ABC) mainly consists of a DC–DC converter and its auxiliary circuits. A three-phase converter (MDC) is used to drive the motor. Since all of the parts of the circuit have only one function, these three power converters are indispensable, which increases the volume, weight, and cost of EVs. In addition, for single-phase and three-phase power supplies, single-phase and three-phase chargers are needed, which is not convenient for users.

To solve the above problems, an integrated multifunctional topology is proposed in this paper. Figure 2 shows the structure of the proposed topology. It mainly consists of a motor driving converter ($Q_1 \sim Q_6$), two H-bridge converters ($Q_7 \sim Q_{10}$ and $Q_{11} \sim Q_{14}$), three inductors (L_a, L_b, and L_{aux}), and four additional relays (M_a, M_b, M_c, and M_d). The motor driving converter (MDC) is composed of three bridges. The first bridge and the second bridge form a front-end full-bridge converter (FE-FBC) and the third bridge forms a middle-end half-bridge converter (ME-HBC). The two H-bridge converters ($Q_7 \sim Q_{10}$ and $Q_{11} \sim Q_{14}$) constitute a back-end full-bridge converter (BE-FBC). In this paper, v_{dc} represents the DC-link voltage, v_{tra} represents the voltage of the traction battery, v_{aux} represents the voltage of the auxiliary battery, v_{Caux} represents the voltage of the capacitor C_{aux}, i_{Laux} represents the current flowing through the inductor L_{aux}, and i_{tra} represents the current flowing through the traction battery.

As a whole, the MDC has three main functions. It serves as a three-phase rectifier for traction battery charging, as a three-phase inverter to feed energy back to the grid, and as a three-phase inverter to drive the motor. The FE-FBC is used as an AC–DC converter for traction battery charging and as a DC–AC inverter for traction battery discharging. The ME-HBC has two important functions. It serves as a buck-type APD circuit for traction battery charging, and as

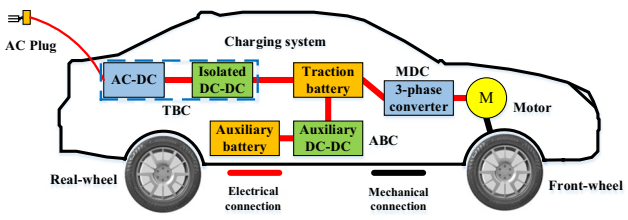

Fig. 1 Schematic of a conventional on-board charger

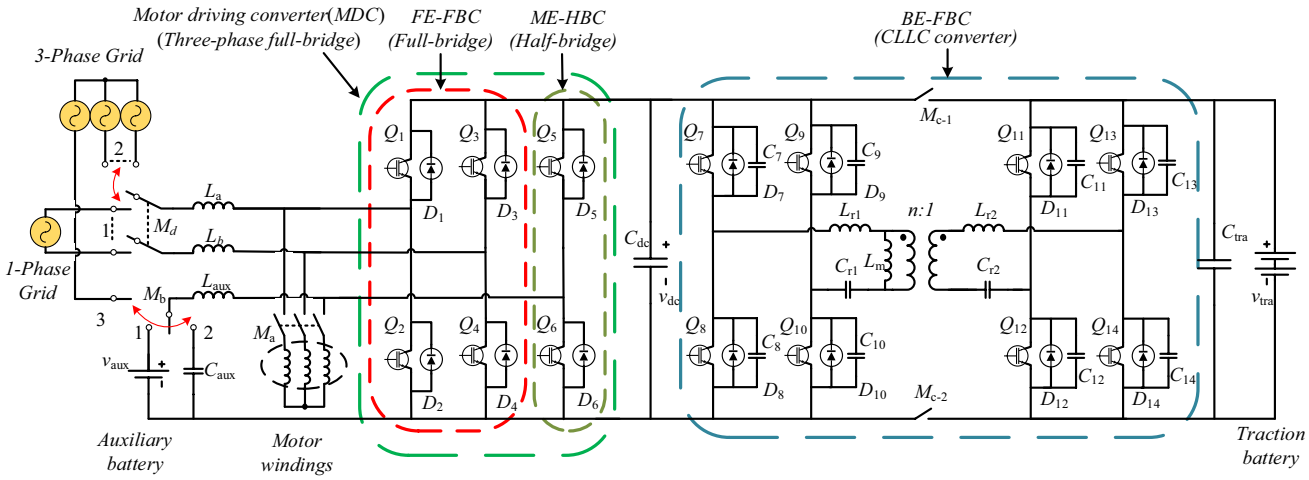

Fig. 2 Circuit diagram of the proposed integrated topology

a buck converter for auxiliary battery charging. The galvanic isolation of this topology is the responsibility of the BE-FBC. When the BE-FBC is operated in the G2V/V2G mode, it isolates the traction battery from the grid, and when it is operated in the T2A mode, it isolates the auxiliary battery from the traction battery, which improves the safety and performance of the topology. The specific operation states are described in the next section.

2.2 Operation states of the proposed topology

As shown in Fig. 2, when M_d switches to "1", M_b switches to "2", the other relays are turned off, and the circuit is connected to the single-phase grid. The FE-FBC is used as a single-phase rectifier to realize unit power factor operation. For eliminating second-order ripple power, the ME-HBC, the inductor L_{aux}, and the capacitor C_{aux} constitute a buck-type active power decoupling (APD) circuit. When the state-of-charge (SOC) of the traction battery is low, the traction battery is charged and power flows from the grid to the traction battery [G2V(1P)]. The role of the BE-FBC is to isolate the traction battery from the power grid. In addition, energy can also be fed back into the single-phase grid from the traction battery through the BE-FBC and the FE-FBC [V2G(1P)].

When M_d switches to "2", M_b switches to "3", the other relays are turned off, and the circuit is connected to the three-phase grid. At this time, the MDC is operated as a three-phase converter. The topology can realize a bidirectional energy flow which is similar to being operated in the single-phase mode [G2V(3P) and V2G(3P)].

In addition, when the auxiliary battery needs to be charged, M_b switches to "1" and the other relays are turned off. The traction battery charges the auxiliary battery through the ME-HBC and the BE-FBC. At this point, the ME-HBC controls the charging voltage and current of the auxiliary battery. Meanwhile, the BE-FBC electrically isolates the auxiliary battery from the traction battery. The electrical power flows from the traction battery to the auxiliary battery (T2A).

When M_a and M_c are turned on, M_b and M_d are turned off. The output current of the traction battery is converted into AC by the MDC to drive the motor. The electrical power flows from the traction battery to the motor (T2M).

The integrated multifunctional topology can implement the functions of G2V (including single-phase and three-phase), V2G (including single-phase and three-phase), T2A, and T2M. Different modes corresponding to the different states of the relays and the switching devices are listed in Table 1.

2.3 Detailed operation modes of the proposed integrated topology

2.3.1 Mode I: traction battery is charged [G2V(1P) and G2V(3P)]

When the topology circuit is connected to a single-phase grid for charging, a schematic of the proposed single-phase charging system with APD is shown in Fig. 3a. According to [15], the instantaneous input power P_{in} of the MDC can be expressed as

$$P_{in} = \frac{U_{ac}I_{ac}}{2}\cos\varphi - P_k \times \sin(2\omega t - 2\varphi + \phi) \tag{1}$$

where U_{ac} and I_{ac} are the amplitudes of the gird voltage and the output current, ω is the grid angular frequency, φ is the angle between the gird voltage and the output current,

$$P_k = \sqrt{\frac{U_{ac}^2 I_{ac}^2}{4}\cos^2\varphi + \left(\frac{\omega L I_{ac}^2}{2} - \frac{U_{ac}I_{ac}}{2}\sin\varphi\right)^2},$$

$$\phi = \tan^{-1}\frac{\frac{U_{ac}I_{ac}}{2}\cos\varphi}{\frac{\omega L I_{ac}^2}{2} - \frac{U_{ac}I_{ac}}{2}\sin\varphi}, \text{and } L = L_a + L_b.$$

Table 1 States of the relays and switching devices in different modes

Operation modes	M_a	M_b	M_c	M_d	Q_1~Q_4	Q_5~Q_6	Q_7~Q_{10}	Q_{11}~Q_{14}
G2V								
G2V(1p)	OFF	2	OFF	1	PWM	PWM	PFM	OFF
G2V(3p)	OFF	3	OFF	2	PWM	PWM	PFM	OFF
V2G								
V2G(1p)	OFF	2	OFF	1	PWM	PWM	OFF	PFM
V2G(3p)	OFF	3	OFF	2	PWM	PWM	OFF	PFM
T2A	OFF	1	OFF	OFF	OFF	PWM	OFF	PFM
T2M	ON	OFF	ON	OFF	PWM	PWM	OFF	OFF

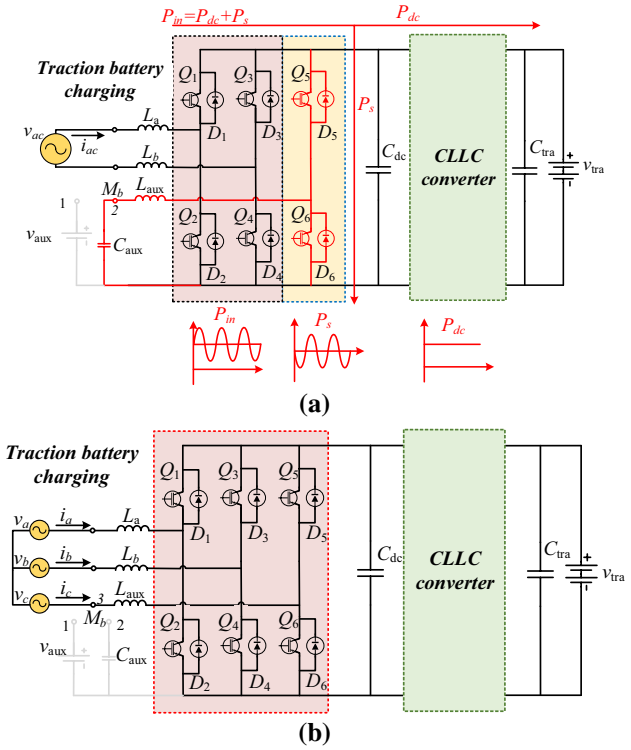

Fig. 3 Traction battery charging modes: **a** G2V(1P); **b** G2V(3P)

The instantaneous power P_{in} consists of two parts: the constant power P_{dc} to charge the traction battery, and the second-order ripple power P_s, which should be absorbed by the decoupling circuit. P_{dc} and P_s can be denoted as

$$P_{dc} = \frac{U_{ac} I_{ac}}{2} \cos \varphi \tag{2}$$

$$P_s = -P_k \times \sin\left(2\omega t - 2\varphi + \phi\right) \tag{3}$$

The ME-HBC, the auxiliary capacitor C_{aux}, and the auxiliary inductor L_{aux} are applied to constitute a buck-type active power decoupling (APD) circuit. It aims to absorb the second-order ripple power P_s as shown in Fig. 3a. The

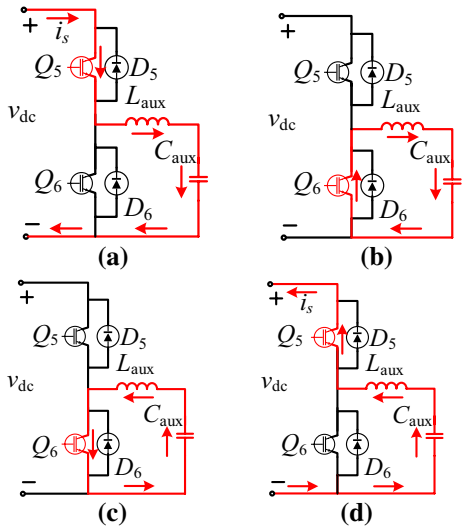

Fig. 4 Operation states of APD: **a** State 1; **b** State 2; **c** State 3; **d** State 4

operation states and waveforms of the APD are analyzed in detail as follows.

Figure 4 shows the operation states of the APD and Fig. 5 shows the main operation waveforms of the APD. When the power $P_{in} > P_{dc}$, the APD works in the buck mode. If Q_6 is turned off and Q_5 is turned on, the ripple current i_s flows through Q_5, the inductor L_{aux}, and the capacitor C_{aux}. It can be seen from Fig. 5 that the ripple current i_s charges L_{aux} and C_{aux}, which causes the inductor current i_{Laux} and capacitor voltage v_{Caux} to rise during this state. Figure 4a shows the path of the current i_s. If Q_5 is turned off and Q_6 is turned on, the energy stored in L_{aux} is transferred into C_{aux} through Q_6, as shown in Fig. 4b. Although the current i_{Laux} is falling, it is still positive. The capacitor voltage v_{Caux} continues to rise.

When the power $P_{in} < P_{dc}$, the APD works in the boost mode, as shown in Fig. 4c and d. When Q_5 is turned off and Q_6 is turned on, the auxiliary capacitor C_{aux} charges the auxiliary inductor L_{aux}, which causes the inductor current i_{Laux} to rise reversely and the voltage across C_{aux} to drop, as shown in Fig. 5. When Q_6 is turned off and Q_5 is

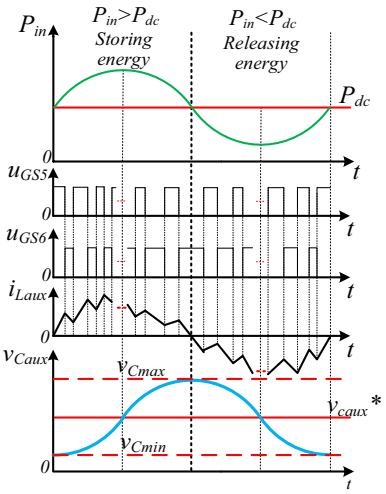

Fig. 5 Operation waveforms of APD

turned on, the inductor L_{aux} and the capacitor C_{aux} release the stored energy to the DC-link through Q_5.

In the G2V mode, the BE-FBC (CLLC converter) is used to electrically isolate the grid from the EV, and it operates at a frequency below the resonant frequency. Under this condition, $Q_7 \sim Q_{10}$ can achieve ZVS turned-on, and $D_{11} \sim D_{14}$ can achieve ZCS turned-off. The design and operating states of the CLLC converter can be found in [19], and will not be analyzed here.

When the proposed topology is connected to a three-phase grid for charging the traction battery, a schematic of the charging system is shown in Fig. 3b. The MDC acts as a three-phase converter to convert the three-phase AC power to DC power with a high power factor. The BE-FBC is used to isolate the traction battery from the three-phase power grid. The operation modes of the BE-FBC are the same as those of the single-phase charging mode.

2.3.2 Mode II: traction battery discharging to the grid [V2G(1P) and V2G(3P)]

The energy stored in the traction battery can be fed back to the grid. When the proposed topology is set to the single-phase mode, the DC-link voltage is regulated by the BE-FBC with pulse frequency modulation (PFM). Then, the FE-FBC is applied to feed the energy back to the single-phase grid. The energy can also be fed back to the three-phase grid when the topology is set to the three-phase mode. The operation states of the circuit in the V2G mode are almost the same as those in the G2V mode. The only difference is that the direction of the energy flow is opposite. Therefore, the operation states of the V2G are not analyzed here.

2.3.3 Mode III: auxiliary battery is charged by the traction battery (T2A)

As shown in Fig. 6, the auxiliary battery can be charged by the traction battery, in which case the ME-HBC is used as a buck converter. The BE-FBC is used to ensure the galvanic isolation between them.

2.3.4 Mode IV: traction battery driving the motor (T2M)

When an electric vehicle is running, the motor driving converter (MDC) is used to drive the motor by connecting to the traction battery, as shown in Fig. 7.

3 Control strategies and parameter design

3.1 Controller design

3.1.1 Control strategy of MDC: G2V, V2G and T2M

When the topology is connected to a three-phase grid, the MDC is operated as a rectifier in the G2V mode and as an inverter in the V2G mode. Figure 8 shows a control block diagram of the MDC for the two modes, and the double closed-loop control strategy adopted in [20]. The DC-link voltage is regulated by the external voltage loop with a conventional PI controller. For the inner current loop, the

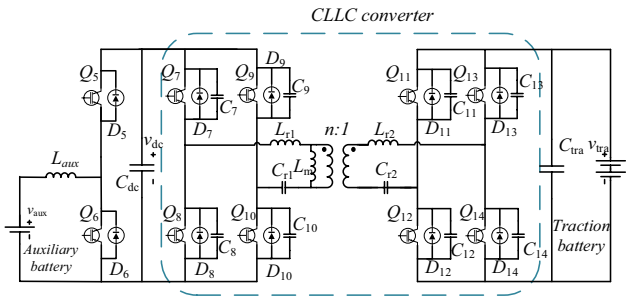

Fig. 6 Schematic of an auxiliary battery being charged

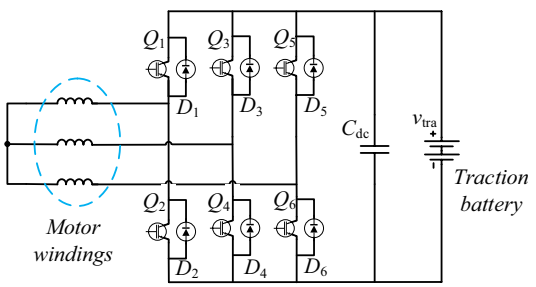

Fig. 7 Circuit schematic for the T2M mode

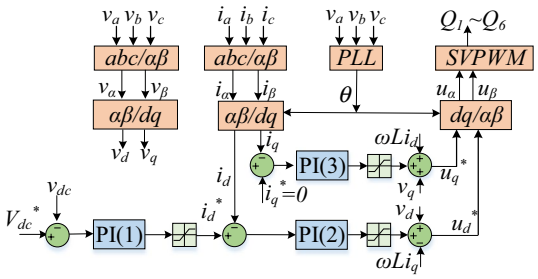

Fig. 8 Control strategy of MDC for the G2V(3P) and V2G(3P) modes

active and reactive powers are decoupled by a *Park-Clarke* transformation. In rotational coordinates, i_d^* and i_q^* represent the active and reactive powers, respectively. To realize unit power factor operation, i_q^* is set to 0, and the output value of the PI controller in the external voltage loop is i_d^*, as shown as follows:

$$i_d^* = K_p^{(1)} * (v_{dc}^* - v_{dc}) + \frac{K_i^{(1)}}{s} * (v_{dc}^* - v_{dc}) \tag{4}$$

Then, u_d^* and u_q^* are output by two PI controllers, whose inputs are the reference dq-axis currents i_d^* and i_q^*, and the actual dq-axis currents i_d and i_q, respectively. According to [21], u_d^* and u_q^* can be given as

$$u_d^* = v_d + K_p^{(2)} * (i_d^* - i_d) + \frac{K_i^{(2)}}{s} * (i_d^* - i_d) - \omega L i_q \tag{5}$$

$$u_q^* = v_q + K_p^{(3)} * (i_q^* - i_q) + \frac{K_i^{(3)}}{s} * (i_q^* - i_q) + \omega L i_d \tag{6}$$

Finally, u_d^* and u_q^* are converted into u_α^* and u_β^*, and input to the *SVPWM* to generate switching signals.

When an electric vehicle is connected to a single-phase grid, the FE-FBC is operated as a rectifier and as an inverter in the G2V and V2G modes, respectively. Its control strategy is almost the same as the three-phase charging mode. A second-order generalized integrator (SOGI) is used to construct a pair of virtual orthogonal signals i_α and i_β, which are calculated as follows [22]:

$$i_\alpha(s) = \frac{k\omega s}{s^2 + k\omega s + \omega^2} * i_{ac}(s) \tag{7}$$

$$i_\beta(s) = \frac{k\omega^2}{S^2 + k\omega s + \omega^2} * i_{ac}(s) \tag{8}$$

where ω is the angular frequency of the grid, and k is quality factor. In addition, v_α and v_β can also be obtained in this way.

When the MDC is operated as an inverter in the T2M mode, its control strategy is shown in Fig. 9. Similar to its operation in the G2V/V2G mode, the conventional double closed-loop control strategy is adopted. This control strategy was presented in [23] and will not be analyzed in this paper.

3.1.2 Control strategy of ME-HBC: APD and T2A

The ME-HBC, the inductor L_{aux}, and the capacitor C_{aux} can be used as an APD circuit to eliminate ripple power or as a buck converter for auxiliary battery charging (T2A). Control blocks for the two modes are shown in Fig. 10.

For the APD, a continuous current (CCM) method is applied in this paper, as shown in Fig. 10a. The ripple current is calculated according to the second-order ripple power P_s. Assuming the DC-link voltage is stabilized at V_0 after power decoupling, i_s can be expressed as

$$i_s = \frac{-P_k \times \sin(2\omega t - 2\varphi + \phi)}{V_0} \tag{9}$$

Due to the operating characteristics of the buck circuit, the voltage of the capacitor C_{aux} must be lower than that of the DC-link. Therefore, an additional voltage control loop is needed, as shown in Fig. 10a. Since the given value i_{Laux}^* is the alternating component, a PR controller is used to control the inductance current i_{Laux} to track i_{Laux}^*.

For the T2A mode, two PI controllers are applied to regulate the auxiliary battery voltage v_{aux} and the inductor current

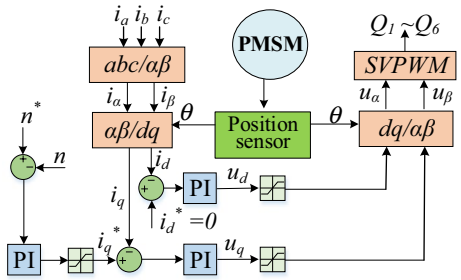

Fig. 9 Control strategy of the MDC for T2M modes

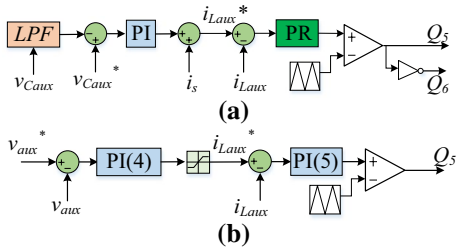

Fig. 10 Control strategy of the ME-HBC: **a** APD; **b** T2A

i_{Laux}, as shown in Fig. 10b. Generally, the reference current $i_{Laux}{}^{*}$ and the duty cycle D_{T2A} for Q_5 are calculated by PI controllers as follows:

$$i^*_{Laux} = K_p^{(4)} * (v^*_{aux} - v_{aux}) + \frac{K_i^{(4)}}{s} * (v^*_{aux} - v_{aux}) \tag{10}$$

$$D_{T2A} = K_p^{(5)} * (i^*_{Laux} - i_{Laux}) + \frac{K_i^{(5)}}{s} * (i^*_{Laux} - i_{Laux}) \tag{11}$$

3.1.3 Control strategy of BE-FBC: G2V, V2G and T2A

The BE-FBC is used to ensure electrical isolation in the G2V, V2G, and T2A modes, which is extremely important. Regardless of whether the charger is connected to a single-phase or a three-phase grid, the BE-FBC has the same operation states. Its control strategies are shown in Fig. 11. In the G2V mode, the EV is charged by a combination of the constant current mode (CC) and the constant voltage mode (CV) mode, as shown in Fig. 11a. When the SOC of the traction battery is lower than a preset value, it operates in the CC mode. To keep the charging current constant, a PI controller is used. The switching frequency f_{G2V} of $Q_7 \sim Q_{10}$ is generated by the PI controller as follows:

$$f_{G2V} = K_p^{(6)} * (i^*_{tra} - i_{tra}) + \frac{K_i^{(6)}}{s} * (i^*_{tra} - i_{tra}) \tag{12}$$

When the SOC is higher than the preset value, the operation mode is changed from the CC mode to the CV mode. At this time, the charging current is no longer constant. However, the charging voltage remains constant. The reference of the battery charging current $i_{tra}{}^{*}$ can be obtained from the PI controller as

$$i^*_{tra} = K_p^{(7)} * (v^*_{tra} - v_{tra}) + \frac{K_i^{(7)}}{s} * (v^*_{tra} - v_{tra}) \tag{13}$$

As shown in Fig. 11b, only the CV mode is applied to keep the DC-link voltage stable in the V2G and T2A modes.

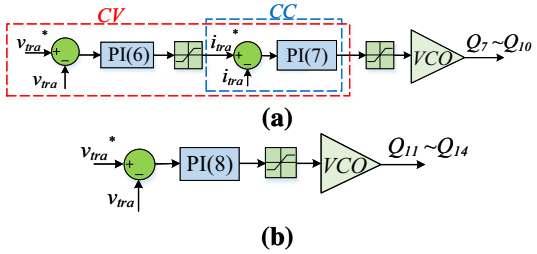

Fig. 11 Control strategy of the BE-FBC: **a** G2V; **b** V2G and T2A

The switching frequency f_{V2G} for $Q_{11} \sim Q_{14}$ is calculated as follows:

$$f_{V2G} = K_p^{(8)} * (v^*_{tra} - v_{tra}) + \frac{K_i^{(8)}}{s} * (v^*_{tra} - v_{tra}) \tag{14}$$

3.2 Inductor and capacitor design

The inductor L_{aux} plays different important roles. The design of L_{aux} needs to take the two conditions into account. For the APD, from the analysis above, it should be operated in the continuous conduction mode (CCM), and the lower limit of L_{aux} can be obtained as [16]

$$L_{aux} > \frac{T_s(v_{dc}v_{Caux} - v_{Caux}^2)}{2\bar{i}_s v_{dc}} \tag{15}$$

where T_s represents the switching cycle, and $\bar{i}_s$ is the average current of the inductor in one switching cycle.

In the T2A mode, to ensure that the ripple current of the inductance meets certain requirements:

$$L_{aux} \geq \frac{(v_{dc} - v_{tra})v_{tra}T_s}{v_{dc}I_{ave}\delta} \tag{16}$$

where δ is the pulsation rate of the current.

For the APD circuit, the capacitor C_{aux} is used to store the ripple energy E_c, which can be obtained by integration:

$$E_c = \int P_k \sin(2\omega t - 2\varphi + \phi)dt = \int C_{aux}\frac{dv_{Caux}}{dt}v_{Caux}dt \tag{17}$$

The capacitance of C_{aux} can be obtained as [16]

$$C_{aux} \geq \frac{2P_k}{\omega v_{Caux\_pek}^2} \tag{18}$$

where ω is the angular frequency, and v_{Caux_pek} is the peak voltage of the capacitor C_{aux}.

4 Experimental verification

To verify the effectiveness of the proposed topology under its different operating modes, a 1.4 kW prototype platform was built as shown in Fig. 12. Its specifications are given in Table 2. IGBTs (BSM50GB60DLC) manufactured by Infineon are used as switches $Q_1 \sim Q_6$, and MOSFETs (C2M0040120D) manufactured by CREE are applied for $Q_7 \sim Q_{14}$. A DSP (TMS320F28335) is adopted for the controller. An oscilloscope (DLM3024) is used to analyze the experimental waveforms. A permanent magnet synchronous motor (PMSM) is used as the drive motor.

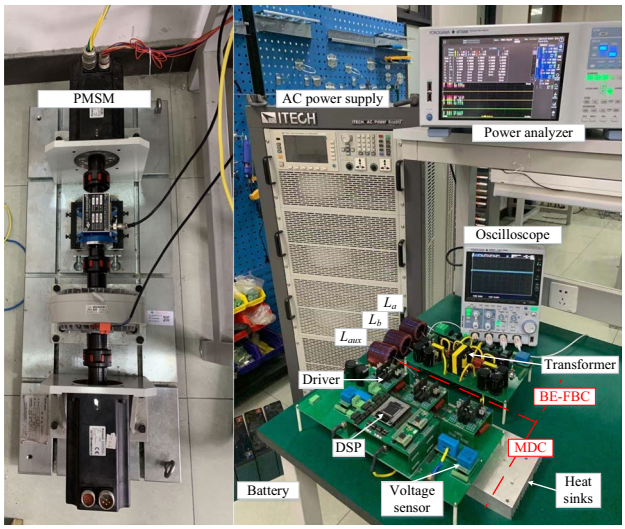

Fig. 12 Prototype platform and laboratory workbench

Table 2 Experimental parameter design

Parameter	Symbol	Specification
Traction battery	v_{tra}	60 V
Auxiliary battery	v_{aux}	24 V
Transformer	n	12:6
Resonant inductor	L_{r1}, L_{r2}	12 μH, 4 μH
Resonant capacitance	C_{r1}, C_{r2}	0.832 μF, 3.33 μF
Magnetizing inductor	L_m	73 μH
Inductor	L_{aux}, L_a, L_b	2 mH
DC-link capacitor	C_{dc}	300 μF
Auxiliary capacitor	C_{aux}	300 μF

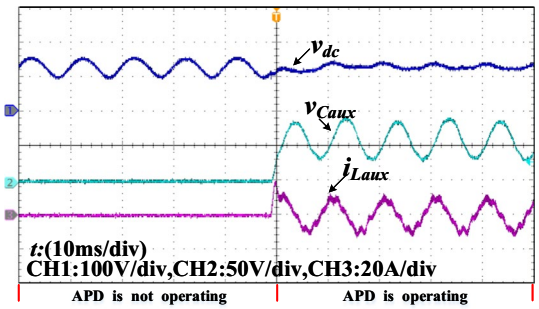

Fig. 13 Experiment results of the APD including the DC-link voltage (v_{dc}), the voltage of the auxiliary capacitor (v_{Caux}), and the current of the auxiliary inductor (i_{Laux})

Figure 13 shows experimental waveforms of the APD circuit. Before the APD circuit is added, the voltage of the auxiliary capacitor and the current of the auxiliary inductor are both zero. At first, the second-order ripple voltage of the DC-link is very large, and its peak-to-peak value reaches 60 V. After the APD circuit is adopted, the second-order ripple voltage greatly decreases from 60 to 12 V, and the DC-link voltage is stabilized at about 120 V. Most of the ripple power is absorbed by the auxiliary capacitor. The current flowing through the auxiliary inductor is continuous and its peak value is close to 12A.

Figure 14a–c shows experimental results in the G2V(1P) mode. The proposed circuit is connected to a single-phase power supply. As shown in Fig. 14a, the grid voltage and current are in phase, which achieves unit power factor operation. The output power is approximately 1400 W. Operation waveforms of the high voltage side of the BE-FBC are shown in Fig. 14b. At this point, the operating frequency is about 45 kHz. After the drain-source voltage of Q_8 drops to zero, its drive signal starts to rise. Hence, ZVS is achieved for Q_8. Figure 14c displays operation waveforms of the low voltage side of the BE-FBC. The output voltage of the BE-FBC is about 60 V and ZCS is realized. Figure 14d displays operation waveforms of the G2V(3P) mode. The proposed circuit is connected to a three-phase power supply. The grid voltage and output current are in phase as shown in this figure, and the output power is about 1440 W. The DC-link voltage is stabilized at 120 V, and the input current of the traction battery is 22.5 A. The operation states of the BE-FBC are the same as those in the G2V(1P) mode.

Figure 15a–c shows experiment results in the V2G(1P) mode. The BE-FBC becomes the input stage and the energy is fed back into the grid. Figure 15a shows that the DC-link voltage is stabilized at 120 V and the input power of the grid is about 1200 W. The grid voltage and the output current are opposite in phase. Operation waveforms of the low voltage side of the BE-FBC are shown in Fig. 15b. The switching frequency is close to 50 kHz and ZVS is realized for the low voltage side. Figure 15c displays operation waveforms of the high voltage side of the BE-FBC. The input voltage of the BE-FBC is 60 V and ZCS is achieved for the high voltage side. Figure 15d displays operation waveforms of the V2G (3P) mode. The DC-link voltage is stabilized at 120 V and the output current of the traction battery is about 21 A. The BE-FBC is operated in the same states as the V2G(1P) mode.

Figure 16 shows experiment results in the T2A mode. Figure 16a shows that the DC-link voltage is about 110 V. The output current of the traction battery is about 9 A, and the input current of the auxiliary battery is approximately 21 A. Figure 16b displays operation waveforms of the low voltage side of the BE-FBC. Its switching frequency is about 55 kHz, which is higher than the resonant frequency. Figure 16c shows that the resonant current is distorted and that the diode current of the high voltage side is forced to drop to zero by the drain-source voltage. ZCS is not achieved for the high voltage side.

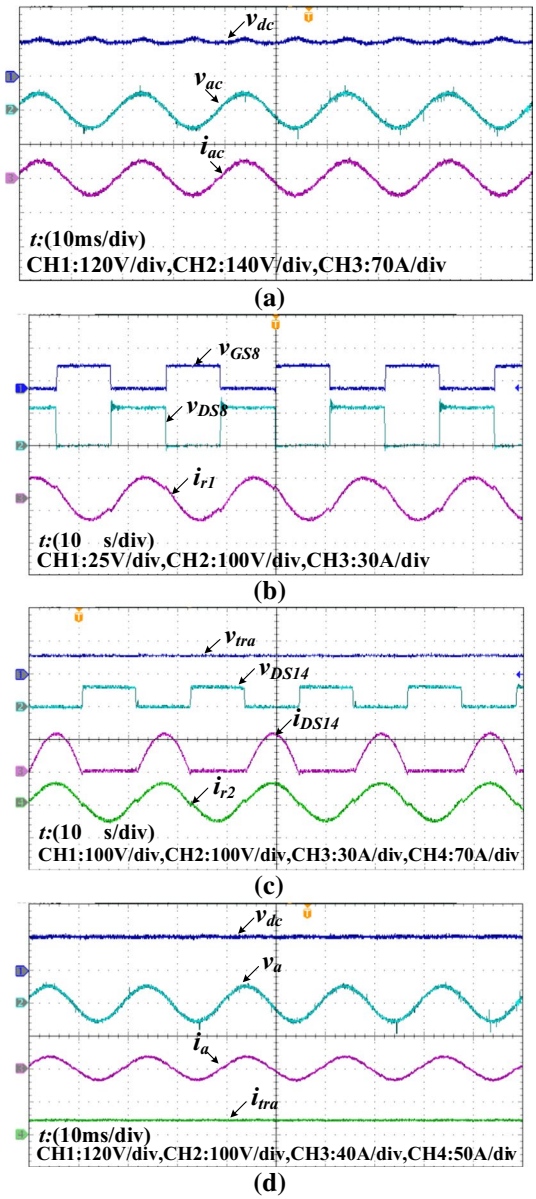

Fig. 14 Experiment results of G2V [(**a**), (**b**), and **c** show experimental results of G2V(1P); and **d** shows experimental results of G2V(3P)]: **a** DC-link voltage (v_{dc}), grid voltage (v_{ac}), and output current (i_{ac}); **b** gate signal for Q_8 (v_{GS8}), voltage across Q_8 (v_{DS8}), and resonance current of the high voltage side (i_{r1}); **c** voltage of the traction battery (v_{tra}), voltage across Q_{14} (v_{DS14}), diode current through D_{14} (i_{DS14}), and resonance current of the low voltage side (i_{r2}); **d** DC-link voltage (v_{dc}), A phase voltage (v_a), A phase current (i_a), and traction battery charging current (i_{tra})

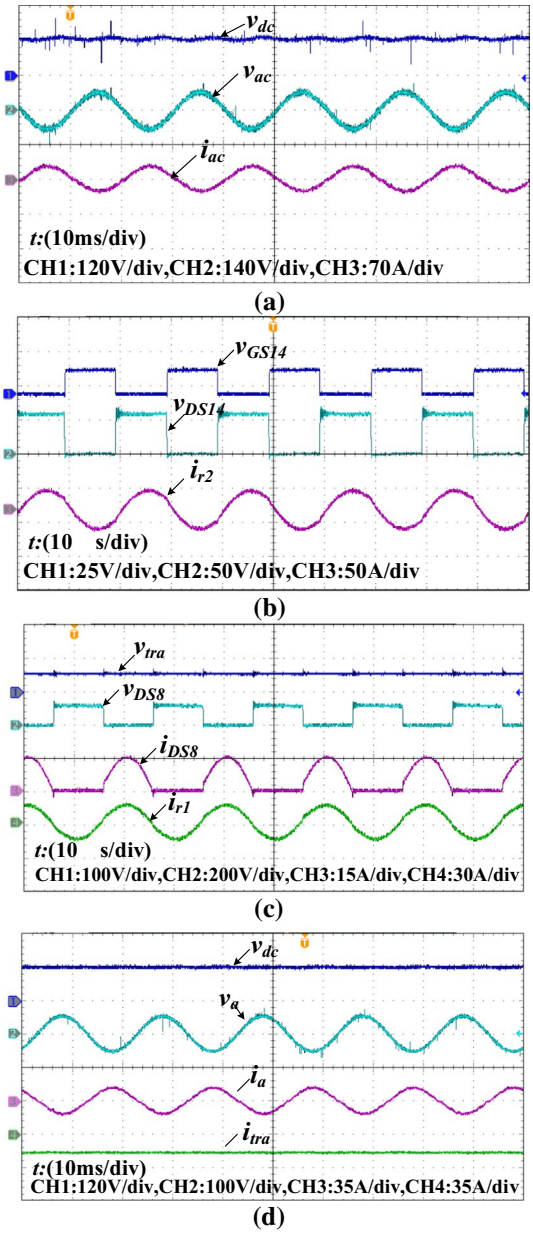

Fig. 15 Experiment results of V2G [(**a**), (**b**), and **c** show experimental results of V2G(1P); and **d** shows experimental results of V2G(3P)]: **a** DC-link voltage (v_{dc}), grid voltage (v_{ac}), and output current (i_{ac}); **b** gate signal for Q_{14} (v_{GS14}), voltage across Q_{14} (v_{DS14}), and resonance current of the low voltage side (i_{r2}); **c** voltage of the traction battery (v_{tra}), voltage across Q_8 (v_{DS8}), diode current through D_8 (i_{DS8}), and resonance current of the high voltage side (i_{r1}); **d** DC-link voltage (v_{dc}), A phase voltage (v_a), A phase current (i_a), and traction battery discharging current (i_{tra})

Figure 17 shows experiment results in the T2M mode. The current of the three-phase windings of the PMSM is shown in Fig. 17a, and the peak value of the current is about 6 A. According to Fig. 17b, the voltage of the traction battery is 60 V and the output current is about 5 A. The PMSM rotates at about 500 r/min and its torque is about 5.2 N.m. The motor is in good working condition.

Figure 18 displays the efficiency of the proposed topology under different modes. Figure 18a displays the efficiencies of the G2V(1P) and the G2V(3P). In mode I, the efficiencies of the G2V(1P) and the G2V(3P) are over 90%. It can be seen that they reach 94.5% and 95.5%, respectively. The efficiency of the G2V(1P) is lower than that of the G2V(3P)

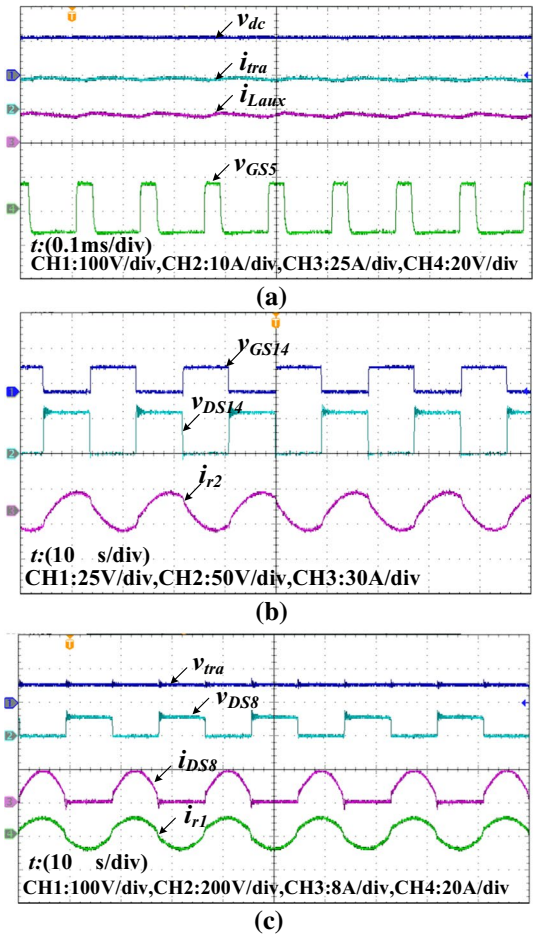

Fig. 16 Experiment results of T2A: **a** DC-link voltage (v_{dc}), output current of the traction battery (i_{tra}), input current of the auxiliary battery (i_{Laux}), and gate signal for Q_5 (v_{GS5}); **b** gate signal for Q_{14} (v_{GS14}), voltage across Q_{14} (v_{DS14}), and resonance current of the low voltage side (i_{r2}); **c** voltage of the traction battery (v_{tra}), voltage across Q_8 (v_{DS8}), diode current through D_8 (i_{DS8}), and resonance current of the high voltage side (i_{r1})

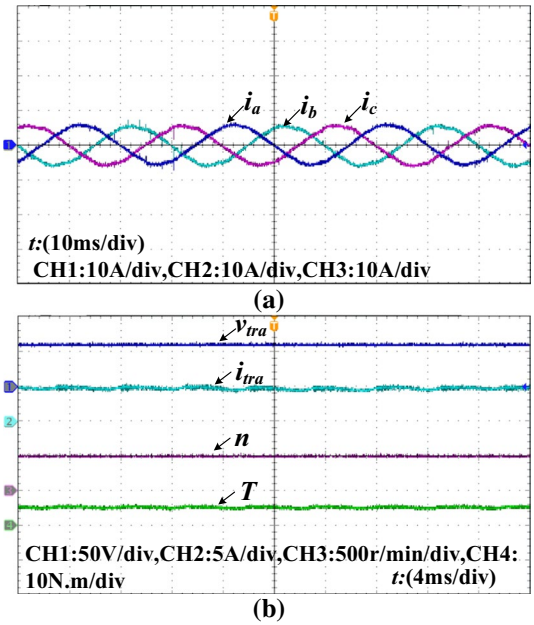

Fig. 17 Experiment results of T2M: **a** current of the three-phase windings of the motor; **b** voltage of the traction battery (v_{tra}), output current of the traction battery (i_{tra}), rotation speed of the motor (n), and the torque of the motor (T)

due to the power losses of the APD circuit. When the proposed charger works in mode II, the efficiency of the V2G(1P) and the V2G(3P) are less than those in mode I, as shown in Fig. 18b. This is mainly caused by the reverse operation of the BE-FBC. The amplitude of the excitation current on the low voltage side of the transformer during reverse operation is n times the amplitude of the excitation current on the high voltage side of the transformer during forward operation, which increases the conduction losses of the switches $Q_{11} \sim Q_{14}$. In addition, the increase in the switching frequency also results in additional power loss. Figure 18c shows the efficiency of the T2A. In this mode, the switching frequency of the BE-FBC is 55 kHz. The efficiency is between 89 and 93%. With an increase of power, the efficiency also increases. The efficiency of the T2A is lower than that of the G2V and the V2G. This is mainly due to the failure to achieve ZCS and low power.

5 Comparison with other topologies

The topology proposed in this paper is compared with the topologies presented in [8, 10], and [11] as well as the conventional topology to demonstrate that it has the advantages of fewer components, higher security, and so on.

The topology of the conventional single-phase bidirectional TBC is shown in Fig. 19, while the topologies of the conventional ABC and MDC are the same as those shown in Figs. 6 and 7 in Sect. 2.3, respectively.

The proposed topology in this paper integrates the TBC, the ABC, and the MDC into one system. The topologies proposed in [8, 10], and [11] lack either the ABC or the MDC. For a more accurate comparison, the missing circuit is added. In addition, it is assumed that in the conventional TBC and ABC topologies, the CLLC converter is used to guarantee electrical isolation, the IGBT is used as a power electronic switch, the components with the same functionality are of the same models, and the cables are ignored due to their small size in all of the topologies.

There are two main types of capacitors. In the conventional single-phase TBC, the buck electrolytic capacitor C_b is connected in parallel to the DC-link to eliminate the

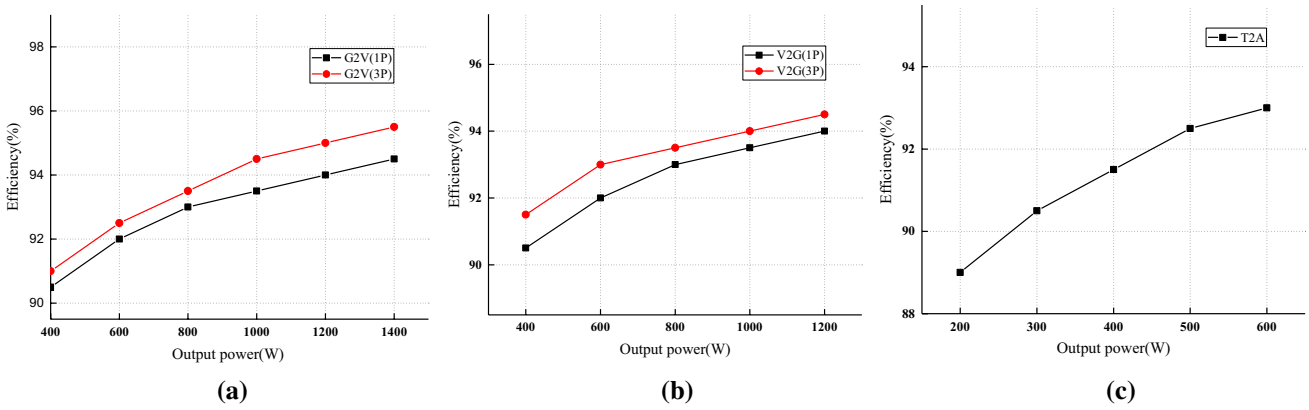

Fig. 18 Efficiency of the proposed integrated topology: a Mode I; b Mode II; c Mode III

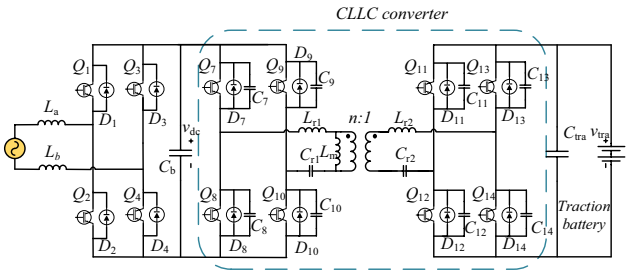

Fig. 19 Conventional topology of a single-phase bidirectional TBC employing a CLLC converter

second-order ripple power. The capacitance value of the capacitor can be calculated [15] by the following equation:

$$C_b = \frac{\sqrt{P_k^2 + ((2\omega L P_k^2 / U_{ac}^2 \cos^2\varphi) - P_k \tan\varphi)^2}}{2 v_{dc} \Delta v_{dc} \omega} \tag{19}$$

where Δv_{dc} is the permissible fluctuation range of the DC-link voltage. On the other hand, the small capacity capacitor C_{dc} is adopted in the proposed topology due to the APD circuit. Table 3 presents a comprehensive comparison of the proposed circuit, the circuits proposed in [8, 10], and [11] as well as the conventional circuit.

A power frequency transformer is used for electrical isolation instead of a CLLC converter in [8]. This reduces the number of switches. However, it greatly increases the volume of the device due to the large size of the transformer. In addition, when the traction battery is charged or discharged, the proposed topology can be configured to the single-phase

Table 3 Comparison with other topologies

	Component	Conventional TBC + ABC + MDC	TBC + ABC in [8], MDC added	TBC + ABC in [10], MDC added	TBC + MDC in [11], ABC added	Proposed TBC + ABC + MDC
Number of components	IGBT	14	7	9	10	7
	Inductor	3	3	3	0	3
	Capacitor (1)	1	1	1	1	0
	Capacitor (2)	4	3	3	1	3
	Relay	0	2	1	4	4
	Heat sink	14	7	9	10	7
	Driver	14	7	9	10	7
	Voltage sensor	7	7	7	4	7
	Current sensor	3	3	1	5	3
Isolation ability		TBC and ABC	ABC	TBC and ABC	ABC	TBC and ABC
Operation modes		Single-phase	Single-phase	Single-phase	Single-phase	Single-phase or three-phase

mode or the three-phase mode, while the other topologies can only work in the single-phase mode. Furthermore, the topologies proposed in [8] and [11] are only capable of electrical isolation when the auxiliary battery is charged. The topology proposed in this paper is capable of electrical isolation when the traction battery is charged or discharged, and when the auxiliary battery is charged. When compared with other topologies, the proposed topology circuit has the advantages of fewer components, a higher safety factor, and more functions.

6 Conclusion

An integrated multifunctional power converter with on-board charging and driving capabilities is presented in this paper. A TBC, an ABC, and an MDC are integrated into a single topology by sharing power electronic devices and components. The number of power electronic devices, capacitors, and inductors used in this topology is less than that in conventional topologies. This paper completes the following work.

1) The proposed topology can achieve a total of four operating modes, which is a great convenience for users. The different operation modes can utilize the same circuit components.
2) For the G2V and V2G modes, the integrated topology can be connected to either a three-phase grid or a single-phase grid. Second-order ripple power can be effectively eliminated when the traction battery is charged by a single-phase system.
3) For the G2V, V2G and T2A modes, the CLLC converter is responsible for ensuring galvanic isolation among the grid, the traction battery, and the auxiliary battery, which provides a high level of system security.
4) This paper describes the four operation modes of the proposed topology and the working principle of the APD circuit, as well as the theoretical analysis and parameter design of the controller in detail. The validity of the proposed topology is verified by experimental results.

Acknowledgements Supported by "the Fundamental Research Funds for the Central Universities" under Grant no. 2018QNA07.

References

1. Ghorbani, R., Bibeau, E.: On conversion of hybrid electric vehicles to plug-in. IEEE Trans. Veh. Technol. **59**(4), 2016–2020 (2010)
2. Hajimiragha, A., Canizares, C.A., Fowler, M.W., Elkamel, A.: Optimal transition to plug-in hybrid electric vehicles in ontario, canada, considering the electricity grid limitations. IEEE Trans. Ind. Electron. **57**(2), 690–701 (2010)
3. Onose, B. A., Hanek, M. A., and Demeter, L. N.: Advanced modular photovoltaic system for Plug-in Small Electric Vehicles (PsEV). In: Proc. Electric Vehicles International Conference (EV), (2017)
4. Hyodo, J., Aoshima, I., Nakamura, A., Saito, N., and Matsuo, R.: Development of electric drive system for small vehicles. In: Proc. World Electric Vehicle Symposium and Exhibition (EVS27), 1429–1432 (2013)
5. Yilmaz, M., Krein, P.T.: Review of battery charger topologies, charging power levels, and infrastructure for plug-in electric and hybrid vehicles. IEEE Trans. Power Electron. **28**(5), 2151–2169 (2013)
6. Zhao, H., Shen, Y., Ying, W.: A single- and three-phase grid compatible converter for electric vehicle on-board chargers. IEEE Trans. Ind. Electron. **35**(7), 7545–7562 (2020)
7. Erb, D. C., Onar, O. C., and Khaligh, A.: Bi-directional charging topologies for plug-in hybrid electric vehicles. In: Proc. IEEE Appl. Power Electron. Conf. Expo., 2066–2072 (2010)
8. Pinto, J.G.: Vítor monteiro, and henrique gonçalves: onboard reconfigurable battery charger for electric vehicles with traction-to-auxiliary mode. IEEE Trans. Veh. Technol. **63**(3), 1104–1116 (2014)
9. Yang, S. Y., Chen, H., Yu, D. S. and Huang, J.: An integrated multifunctional battery charger with three-phase charging for plug-in electric vehicles. In: Proc. IPEMC2020-ECCE Asia, 834–839 (2020)
10. Kim, S., Kang, F.-S.: Multifunctional onboard battery charger for plug-in electric vehicles. IEEE Trans. Ind. Electron. **62**(6), 3460–3472 (2015)
11. Xiao, Y., Liu, C., Yu, F.: an integrated on-board ev charger with safe charging operation for three-phase IPM motor. IEEE Trans. Ind. Electron. **66**(10), 7551–7560 (2019)
12. Ali, S. Q., Mascarella, D., Joos, G., Coulombe, T. and Cyr, J. M.: Three phase high power integrated battery charger for plugin electric vehicles. In: Proc. 2015 IEEE Veh. Power Propulsion Conf. 1–6 (2015)
13. Sakr, N., Sadarnac, D. and Gascher, A.: A review of on-board integrated chargers for electric vehicles. In: Proc. 2014 16th Eur. Conf. Power Electron. Appl. 1–10 (2014)
14. Khaligh, A., Dusmez, S.: Comprehensive topological analysis of conductive and inductive charging solutions for plug-in electric vehicles. IEEE Trans. Veh. Technol. **61**(8), 3475–3489 (2012)
15. Wang, R.X., Wang, F., Boroyevich, D., Burgos, R., Lai, R.: A high power density single-phase PWM rectifier with active ripple energy storage. IEEE Trans. Power Electron. **26**(5), 1430–1443 (2011)
16. Zhang, Y., Fang, J., Gao, F., Gao, S.H., Rogers, D.J., Zhu, X.: Integrated high and low frequency current ripple suppressions in a single-phase onboard charger for EVs. IEEE Trans. Power Electron. **36**(2), 1717–1729 (2021)
17. Chao, K.-H. and Cheng P.-T.: Decoupling Methods for single-phase three-poles AC/DC converters. In: Proc. IEEE Energy Conversion Congress and Exposition 3742–3747 (2009)
18. Sun, Y., Liu, Y., Su, M., Xiong, W., Yang, J.: Review of Active Power Decoupling Topologies in Single-Phase Systems. IEEE Trans. Power Electron. **31**(7), 4778–4794 (2016)
19. Jung, J.-H., Kim, H.-S., Ryu, M.-H., Baek, J.-W.: Design methodology of bidirectional CLLC resonant converter for high-frequency isolation of DC distribution systems. IEEE Trans. Power Electron. **28**(4), 1741–1755 (2013)
20. Wei, J., Chen, J., Wang, Y., Liu, P., Zhou, B.: Coupling property analysis of the on-board battery-charging system based on DSEM in the charging mode. IET Electr. Power Appl. **14**(12), 2312–2321 (2020)

21. Xiang, Y., Pei, X., Huang, S., Li, B., Chen, X., Zhu, X. and Zhang, Y.: A novel control method of virtual orthogonal circuit of single-phase PWM rectifier based on complex vector theory. In: Proc. International Conference on Electrical Machines and Systems (ICEMS), 115–121 (2016)
22. Prakash, S., Singh, J. K., Behera, R. K. and Mondal, A.: Comprehensive analysis of SOGI-PLL based algorithms for single-phase system. In: Proc. National Power Electronics Conference (NPEC), 11–18 (2019)
23. Bae, B.-H., Sul, S.-K., Kwon, J.-H.: Implementation of sensorless vector control for super-high-speed PMSM of turbo-compressor. IEEE Trans. Ind. Appl. **39**(3), 811–818 (2003)

He Cheng received his B.S. and Ph.D. degrees from the School of Information and Electrical Engineering, China University of Mining and Technology, Xuzhou, China, in 2010 and 2015, respectively. In 2017, he became an Associate Professor in the School of Electrical and Power Engineering, China University of Mining and Technology, Xuzhou, China. His current research interests include electrical motor drives, motor design and control, electric vehicles, and on-board chargers for plug-in electric vehicles.

Wuhui Wang received his B.S. degree in Electrical Engineering from the College of Water Resources and Architectural Engineering, Northwest A&F University, Shanxi, China, in 2016. He is presently working towards his M.S. degree in Electrical Engineering at the China University of Mining and Technology, Xuzhou, China. His current research interests include integrated on-board chargers.

Hailong Liu received his B.S. degree from the School of Information and Electrical Engineering, China University of Mining and Technology, Xuzhou, China, in 2019, where he is presently working towards his M.S. degree. His current research interests include plane transformers and CLLLC converters.

Shiyang Yang received his M.S. degree in Electrical Engineering from the China University of Mining and Technology, Xuzhou, China, in 2021. He is presently working for the State Grid Corporation of China, Beijing, China. His current research interests include multifunctional power electronic converters and LLC converters.